

preprint; final version published as Physical Review B 66, 224303 (2002).

Temperature dependence of infrared-active phonons in CaTiO_3 : a combined spectroscopic and first-principles study

V. Železný,¹ Eric Cockayne,² J. Petzelt,¹ M.F. Limonov,³
D.E. Usvyat,³ V.V. Lemanov,³ and A.A.Volkov⁴

¹*Institute of Physics, ASCR, Na Slovance 2, 18221 Prague 8, Czech Republic*

²*Ceramics Division, National Institute of Standards and Technology,
Gaithersburg, Maryland 20899-8520, USA*

³*A.F. Ioffe Physical-Technical Institute, 194021 St. Petersburg, Russia*

⁴*Institute of General Physics, Moscow, Russia*

Abstract

Spectroscopic studies involving dielectric, submillimeter, infrared and Raman measurements were performed on a CaTiO_3 single crystal, covering a broad spectral range (static to 10 THz) at temperatures from 6 K to 300 K. The results show mode softening characteristic of an incipient ferroelectric with $T_c \approx -105$ K. A signature of the soft mode is seen in the Raman spectra, even though the soft modes are not Raman-active to first order. First-principles calculations were used to identify the phonons responsible for the spectral features. Many of the major features are due to phonons in orthorhombic CaTiO_3 that are associated with zone-boundary phonons of the cubic perovskite phase.

PACS numbers: 77.84 Dy, 77.22 Ch, 78.30 Hv, 63.20 Dj

I. INTRODUCTION

Calcium titanate CaTiO_3 (CTO) is well known as mineral perovskite who gave its name to the large and very important family of ABO_3 compounds. These materials are important not only for their technical applications but also for fundamental research. Their simple crystal structure, and the variety of structural phase transitions which they display, make them suitable for experimental study and for testing theoretical models.

Great progress has been achieved during recent years in understanding lattice dynamics, dielectric properties and phase transition phenomena in the oxide perovskites using first-principles calculations[1–7]. The relatively simple sequences of phase transitions in PbTiO_3 , BaTiO_3 , KNbO_3 , and SrTiO_3 have been already reproduced using Monte-Carlo simulations, whereas the complex sequences in CTO or NaNbO_3 have not yet been successfully reproduced[8].

The prototype perovskite structure is cubic (space group $Pm\bar{3}m$, O_h^1 , $Z = 1$), but the room temperature structure of CTO is orthorhombic with a quadrupled unit cell ($Pbmn$, D_{2h}^{16} , $Z = 4$) [9–13]. The deviations from the cubic structure are small, however, and the crystal keeps its pseudocubic character with cell parameters $(a/\sqrt{2}, b/2, c/\sqrt{2}) \approx 3.822 \text{ \AA}$ down to low temperatures. The first evidence for a high-temperature phase transition was found in the 1940s[14], but the problem of the high-temperature structures has recently been the subject of intense study[15–18]. It is now clear that CTO undergoes at least two, but probably three, phase transitions at high temperatures. Increasing the temperature, the first transition appears near 1385 K, into another orthorhombic structure ($Cmcm$, D_{2h}^{17} , $Z_{prim} = 4$, or $Pm\bar{2}n$, D_{2h}^{13} , $Z = 8$), the second one near 1500 K into a tetragonal structure ($I4/mcm$, D_{4h}^{18} , $Z_{prim} = 2$) and the last one near 1580 K into the prototype cubic structure of the $Pm\bar{3}m$, $Z = 1$ symmetry. All the high-temperature phases can be realized from the cubic phase by appropriate TiO_6 octahedra tilting: the tetragonal phase by an anti-phase tilt along one axis ($a^0a^0c^-$ in Glazer’s notation [19, 20]), the intermediate orthorhombic phase by an additional, in-phase, tilt along the second axis ($a^0b^+c^-$) and the room temperature phase by an additional anti-phase tilt, of equal magnitude, along the

third axis ($a^-b^+a^-$ or $a^-a^-c^+$, which corresponds to the space-group symbol $Pbmn$ used throughout this paper). Because the last tilting angle jumps from zero to a finite value, the transition at 1385 K is first-order[15]. From a lattice-dynamical and group-theoretical point of view, the room-temperature phase can be obtained by combining instabilities at the R and M points of the cubic Brillouin zone (corresponding to the anti-phase (-) and in-phase (+) tilts, respectively) [21, 22], but no experimental data on these instabilities are available.

In technical application, CTO is an important constituent of different ceramic solid solutions, which serve as high-quality microwave material for dielectric resonators [23–25]. High permittivity, low dielectric loss, and temperature stability are required for this application. CTO must be mixed with other materials to compensate for the strong temperature dependence of the permittivity of pure CTO. Its permittivity increases upon cooling from 170 at 300 K to approximately 330 near 25 K, where it saturates obeying the Barrett formula [26, 27]. Such behavior is typical of incipient ferroelectrics like SrTiO_3 and KTaO_3 , as pointed out recently by Lemanov *et al.*[26]. As in these materials, no appreciable dielectric dispersion was observed in CTO up to the microwave range. The microwave permittivity above 80 K obeys the Curie-Weiss law with a negative Curie temperature -84 K [28]. Almost all the data were obtained on ceramic polycrystalline samples. Dielectric measurements on a polydomain single crystal were carried out by Linz [27], but the results do not differ appreciably from those for ceramics.

It is natural to expect that a polar soft mode should be responsible for the permittivity behavior in CTO. Using density functional theory, Cockayne and Burton[2] calculated the phonon frequencies for orthorhombic CTO and found a pseudotriplet of polar modes with $\nu \approx 90 \text{ cm}^{-1}$. Cockayne[3] showed that these modes were strongly anharmonic and concluded that their frequencies decreased with decreasing temperature. The most suitable technique for investigating polar modes experimentally is IR reflectivity spectroscopy, because the ac electric field directly couples to the polarization. Room-temperature reflectance data on ceramic samples [29, 30] revealed a low-frequency polar mode near 100 cm^{-1} . Knyazyev *et al.*[31] measured the reflectance at 470 K, 300 K and 110 K and found that the lowest-frequency phonon softened with decreasing temperature. As the CTO structure is cen-

tro-symmetric, the polar modes are not Raman active and indeed micro-Raman studies on small single crystals [32–34] detected no modes below 100 cm^{-1} . On the other hand, a Raman soft mode should be associated with the high-temperature phase transitions. A partial softening of an A_g mode from 150 cm^{-1} down to the value at which it dives into the central (Rayleigh) line has been observed[34] close to the phase transition temperature $T_c=1385\text{ K}$. The Raman data on polycrystals were limited to the frequency range above 100 cm^{-1} [35].

In this work we want to remedy the gaps in the spectroscopic data on CaTiO_3 . We present results of comprehensive spectroscopic study on polydomain single crystals. We report detailed IR data based on reflectivity measurements in the temperature range from 300 K down to 6 K . They were complemented by submillimeter ($7\text{--}13\text{ cm}^{-1}$) transmission measurements and Raman measurements performed on both single crystals and ceramics in the same temperature range. Particular attention was paid to the low-frequency behavior. We have quantitatively established the picture of polar soft phonon mode, but important softening was observed also for a weaker higher-frequency mode folded from the cubic Brillouin zone boundary. Surprisingly, the soft mode behavior was also observable in the Raman spectra of ceramics. By using first-principles calculations, we can identify the symmetries and eigenvalues of the phonons responsible for the observed IR spectra.

II. EXPERIMENTAL[36]

In the past, most measurements on CaTiO_3 were done on ceramic samples. In this work, we concentrate on CaTiO_3 single crystals and compare them with ceramics. Single crystals of CaTiO_3 were grown by the cold crucible method (or so-called skull method) using CaCO_3 and TiO_2 of high purity (i.e. 99.99%) as starting materials. Ceramics samples were prepared with a conventional ceramic technology using the same starting materials. The ceramics were sintered at $1465\text{ }^\circ\text{C}$ and had a relative density of 0.92 of the theoretical value. The samples were cut into rectangular blocks of size $6\times 4.5\times 3\text{ mm}^3$ and their surface was polished to optical quality. A routine examination of the crystal under a polarizing microscope with crossed polarizers revealed a rich domain structure. The domains occur in the

crystal as a consequence of the ferroelastic phase transitions at high temperatures. They can in principle be removed by applying a mechanical stress, but this is practically impossible in this case of large bulk samples as in our case. Near normal reflectance measurements between 30 cm^{-1} and 4000 cm^{-1} were carried out using a Bruker IFS 113v Fourier transform spectrometer. The dielectric function in the frequency range 7 cm^{-1} to 15 cm^{-1} was measured by a backward wave oscillator (BWO) spectrometer. This quasioptical technique measures not only the magnitude of the signal but also its phase and enables one to determine the complex response functions directly without using Kramer-Kronig analysis or model fitting. The Raman experiments were performed using a triple Z-24 Dilor spectrometer and the 514.5 nm line of an Ar laser as an excitation source. The samples were mounted in a continuous helium cryostat in which the temperature could be varied between 6 K and 300 K for infrared and BWO measurements, and in a closed-cycle helium cryostat for Raman scattering.

III. RESULTS

The temperature dependence of the infrared reflectance spectra is shown in Fig 1. The spectra were measured using unpolarized radiation (without polarizers) because the rich domain structure observed in the sample is randomly oriented. In this case we can measure only an average value of reflectance over all domains. The randomness of the domain orientation was also checked by rotating the crystal in polarized radiation beam and no changes in the spectra were found. We discuss the consequences of reflectance averaging in greater detail in the Appendix.

The spectra in Fig. 1 display the characteristic patterns for perovskites and are in reasonable agreement with the early data at room temperature[29, 31]. They consist of three broad “reststrahlen” bands between the strongest transverse optic (TO) and longitudinal optic (LO) modes which presumably correspond to the infrared-active vibrational modes of F_{1u} symmetry in the cubic phase. The first of these bands (TO1 - LO1) is located below 160 cm^{-1} , the second one (TO2 - LO2) at 170 cm^{-1} to 500 cm^{-1} and the third one (TO3 -

LO3) at 550 cm^{-1} to 800 cm^{-1} . Other features, abundantly observed in the spectra, must be due to the additional polar modes activated in the orthorhombic crystal. The most significant feature is the band between 430 cm^{-1} and 500 cm^{-1} . It is quite pronounced and isolated from the other bands, but subsequent analysis of the data shows that it is *not* associated with a cubic perovskite F_{1u} mode. As the temperature is reduced, sharpening of the spectral features and shifts in frequency (mostly to higher frequency) are observed. The first, low-frequency band, however, shows an opposite shift, which is typical for soft modes above a phase transition or incipient phase transition.

IV. DISCUSSION

We used three different ways to analyze our experimental data and evaluate important spectral parameters for understanding the temperature-dependent behavior of CaTiO_3 . In the first approach we describe the spectra by three infrared active modes. Secondly, we tried to find a optimum number of modes for fitting the spectra. Finally we used the Kramers-Kronig analysis to calculate and fit ϵ_1 and ϵ_2 simultaneously.

The most commonly-used fit to dielectric dispersion in ordinary crystals is the “three-parameter model”, where the dielectric function is modeled by the sum for independent damped harmonic oscillators:

$$\epsilon(\nu) = \epsilon_1(\nu) + i\epsilon_2(\nu) = \epsilon_\infty + \sum_i \frac{\Delta\epsilon_i \nu_{iTO}^2}{\nu_{iTO}^2 - \nu^2 + i\gamma_{iTO}\nu}, \quad (\text{IV.1})$$

where ϵ_∞ is the high-frequency (electronic) dielectric constant, $\Delta\epsilon_i$ the oscillator strength of the i -th transverse vibrational mode, ν_{iTO} its frequency, and γ_{iTO} its damping coefficient. It has been shown [37, 38], however, that in the case of broad reflection bands (large LO-TO splitting), it is more accurate to use a “four-parameter fit”:

$$\epsilon(\nu) = \epsilon_1(\nu) + i\epsilon_2(\nu) = \epsilon_\infty \prod_i \frac{\nu_{iLO}^2 - \nu^2 + i\gamma_{iLO}\nu}{\nu_{iTO}^2 - \nu^2 + i\gamma_{iTO}\nu}, \quad (\text{IV.2})$$

which explicitly includes the longitudinal (LO) vibrational frequencies and introduces longitudinal damping parameters. The four-parameter model implicitly contains a frequency-dependent damping coefficient $\gamma_i(\nu)$ for each mode, as reflected by the values γ_{iTO} and γ_{iLO}

for $\nu = \nu_{iTO}$ and ν_{iLO} , respectively. This generalization substantially improves the fit of the broad reflectivity bands. Neglecting damping, the TO oscillator strength $\Delta\epsilon_i$ is given in terms of TO-LO splitting via

$$\Delta\epsilon_i = \frac{\epsilon_\infty}{\nu_{iTO}^2} \frac{\prod_j (\nu_{jLO}^2 - \nu_{iTO}^2)}{\prod_{j \neq i} (\nu_{jTO}^2 - \nu_{iTO}^2)}, \quad (\text{IV.3})$$

The four-parameter model, however, may give an unphysical negative $\epsilon_2(\nu)$ for certain frequencies $\nu > 0$. To avoid this situation, one must either enforce special relationships between the model parameters or else verify directly that $\epsilon_2(\nu)$ is positive for all $\nu > 0$. The infrared reflectivity can be obtained from complex dielectric response $\epsilon(\nu) = \epsilon_1(\nu) + i\epsilon_2(\nu)$ via

$$R(\nu) = \left| \frac{\sqrt{\epsilon(\nu)} - 1}{\sqrt{\epsilon(\nu)} + 1} \right|^2. \quad (\text{IV.4})$$

A Pseudocubic crystal

We restrict ourselves in this subsection to a pseudocubic model, where only three infrared active F_{1u} phonons are assumed, as in the phonon spectrum of the cubic perovskite structure. This approach is *a priori* justified by the small deviations of the orthorhombic CaTiO_3 structure from the ideal perovskite. In this case, very reasonable fits to the reflectivity spectra can be obtained using Eqs. IV.2 and IV.4. The model parameters are obtained by minimizing the root mean square deviation of the reflectivity over the range from 30 cm^{-1} to 1200 cm^{-1} . The fitted spectra are shown and compared with the experimental data in Fig. 1. The lowest frequency mode behaves as a soft mode. Its frequency is 110 cm^{-1} at room temperature and decreases to 77 cm^{-1} at 6 K. The fitted model parameters are presented in Table I. This very rough approximation gives a good description of the frequency dependence of reflectivity and its temperature dependence. It overestimates the static permittivity calculated from the model parameters ($\epsilon(0) = \sum_i \Delta\epsilon_i + \epsilon_\infty$), however, giving a value that increases from 217 at room temperature to 512 at 6 K, compared with the measured low-frequency permittivity values of 170 and 330, respectively. To address this shortcoming a more complex approach is used in the following subsections B and C.

B Optimum fit with 4-parameter model

The fit of the CTO reflectance can be improved, when the orthorhombic symmetry of the material is taken into account and the number of the terms in the factorized dielectric function is increased. The number and the symmetries of the IR-active phonons in orthorhombic CTO can be easily obtained from factor group analysis. Following the site symmetry of atoms in the room-temperature unit cell (4 Ti atoms at 4b, 4 Ca at 4c, 4 O₁ at 4c and 8 O₂ at 8d sites)[10], the vibrational representation in the Γ -point yields $\Gamma_{vibr} = 7 A_g + 8 A_u + 7 B_{1g} + 8 B_{1u} + 5 B_{2g} + 10 B_{2u} + 5 B_{3g} + 10 B_{3u}$. B_{1u} , B_{2u} , and B_{3u} representations are IR active which gives 25 IR-active optic modes (plus 3 acoustic modes). A_g , B_{1g} , B_{2g} , and B_{3g} representations are Raman active, giving 24 Raman modes.

A similar factor group analysis of the zone-center phonons of the high-temperature prototype cubic perovskite phase of CTO yields one F_{1u} acoustic triplet, three F_{1u} IR-active triplets, and one F_{2u} silent triplet. Figure 2 and Table II show the relationship between the symmetries of the cubic and the orthorhombic IR-active modes. Figure 2 interpolates between first-principles phonon frequency results[7] for cubic CTO and orthorhombic CTO. Nine IR-active modes of orthorhombic CTO are grouped into $(B_{1u} + B_{2u} + B_{3u})$ pseudotriplets emanating from IR-active F_{1u} cubic triplets. A pseudodoublet of orthorhombic IR-active modes arise from the cubic F_{2u} triplet: $F_{2u} \rightarrow (\text{silent } A_u + B_{2u} + B_{3u})$. The final fourteen orthorhombic IR modes have their progenitors in the X, M, and R-points of the cubic Brillouin zone and become active due to Brillouin zone folding in the orthorhombic phase. To the extent that the orthorhombic structure is a small perturbation of the cubic one, one expects the nine modes arising from the F_{1u} cubic triplets to be strong and the other sixteen to be weak. All twenty-four orthorhombic Raman modes stem from the X, M and R-points of the cubic Brillouin zone (Table II).

We have found that the minimum number of oscillators required to get a good fit of our spectra is 14. Adding further modes does not improve the quality of the fit. The experimental CTO reflectance and the associated fits at room temperature and at 6 K are shown in Fig 3. The corresponding parameters used in the fit for both temperatures are

given in Table III. Note that the number of oscillators used in the fit is less than the number of IR-active modes determined from group theory. There are several reasons why it is difficult to observe the full spectrum. Some phonons, especially those emanating from Brillouin zone boundary, have such low oscillator strengths that they cannot be detected in the spectra. Overlap of phonons which are close in frequency and which have significant damping also reduces the number of modes which can be resolved. The effective averaging of the reflectance over different domain orientations compounds the above effects (see the Appendix). Finally, the reflectance of CTO is very high (close to 1) for $\nu < 400 \text{ cm}^{-1}$ and the strongly non-linear relation (IV.4) between the reflectivity and the dielectric functions $\epsilon_1(\nu)$ and $\epsilon_2(\nu)$ reduces the accuracy of the fit. These are the most relevant reasons why only 14 phonons can be distinguished in the spectra.

Using 14 oscillators, we obtain $\epsilon(0) = 195$ at $T = 300 \text{ K}$ and $\epsilon(0) = 361$ at room temperature. These values are in very good agreement with experiment.

C Kramer-Kronig analysis

We can calculate the complex dielectric function from the reflectivity using Kramers-Kronig analysis. For this purpose, we need to extend the spectral range of our infrared data by including the complex dielectric function measured by other techniques at submillimeter frequencies, as well as the static permittivity. Very good overlap of the infrared data and those obtained by the BWO spectroscopy (discussed in Section II) and low-frequency dielectric measurements (100 Hz - 1 MHz) enables us to merge all these spectra. We obtain in this way the reflectivity spectrum over a very broad frequency range from 0 to 4000 cm^{-1} . The usual low- and high-frequency extrapolations for dielectrics can be now applied, because the reflectivity on both sides of the spectra is practically constant with no dispersion. In this case Kramers-Kronig analysis gives very reliable results, which confirm the rough estimate made from the reflectance spectra. The real and imaginary parts of the dielectric function ($\epsilon_1(\nu)$ and $\epsilon_2(\nu)$) are given in Fig 4. The pseudocubic character of the sample is apparently demonstrated by three main absorption bands in $\epsilon_2(\nu)$ and the corresponding

dispersion in $\epsilon_1(\nu)$. $\epsilon_2(\nu)$ shows three distinct maxima at 111 cm^{-1} , 157 cm^{-1} , and 549 cm^{-1} . These are close to the values given by Perry *et al.*[29, 30]. They interpreted their spectra in terms of two overlapped phonon triplets at 148 cm^{-1} and 178 cm^{-1} and another split triplet at 549 cm^{-1} . As will be discussed in more detail in section IV E, however, the modes near 157 cm^{-1} actually arise from cubic zone-boundary modes; the true second pseudocubic band is near 220 cm^{-1} , but has accidentally low oscillator strength.

Above 224 cm^{-1} the spectra show only very weak temperature dependence. Below 224 cm^{-1} , however, significant changes appear as temperature changes. The behavior of $\epsilon_1(\nu)$ and $\epsilon_2(\nu)$ in the low-frequency region is shown in detail in Fig 5, where seven modes can be identified. An easy correctness check for the extrapolated optical functions ($\epsilon_1(\nu)$, $\epsilon_2(\nu)$) is to compare them with values measured directly using BWO. Fig 5 shows very good agreement between the calculated curves and the experimental BWO measurements.

A more detailed look at the spectrum shows that the softening process is started by a weak mode at 130 cm^{-1} whose softening has already begun at room temperature. The softening of this mode stops at about 150 K, but triggers a similar process in the lower-frequency modes. This behavior can be understood based on coupling between modes with the same symmetry. Crossing of modes with the same symmetry is forbidden, so if a higher-frequency mode softens more rapidly than a lower-frequency one, the higher mode must eventually repel the lower one and transfer the softening to it. A slight softening of a mode at 180 cm^{-1} can also be observed.

To get more quantitative information about what happens with particular modes, we fitted simultaneously the real and imaginary part of the dielectric function by the sum of damped harmonic oscillators using the three-parameter model (Eq. IV.1). We use the three parameter model rather than the four parameter one because interpretation of the results in terms of oscillator parameters is simpler; furthermore, frequency dependence of damping is less significant when one considers only a small range of frequencies. We easily obtain the temperature dependence of the oscillator parameters in the soft mode spectral range. The results are given in Fig 6 and Table IV. Remarkably, fitting to the K-K analysis reveals an additional low-frequency mode compared with the reflectivity fit by resolving two

components of the split soft triplet emanating from a cubic F_{1u} mode. Another remarkable fact is that also phonon frequencies determined by the 4-parameter fit and K-K analysis are somewhat different as can be seen from Fig 6. This is probably due to nonlinear relation between ϵ and R , and high sensitivity of the parameters to R , when R approaches 1. When we conversely calculate reflectivity from the parameters obtained by fitting the K-K results, the calculated and experimental reflectivity do not match perfectly, although all significant features in the spectrum are observed. The deviations are especially noticeable in the vicinity of the LO frequencies, and occur because the 3-parameter model does not take into account the frequency dependence of the damping as per the discussion following Eq. IV.2.

The static dielectric constant calculated from Kramers-Kronig analysis is in good agreement with the one experimentally measured. This is not a trivial result because it shows that there is no other dispersion between the infrared region and zero frequency. This also means that no central peak excitations exist in CaTiO_3 and that the behavior of the static permittivity is fully determined by the soft mode.

Time-dependent Landau theory predicts that the soft mode frequency should vary with temperature as $\nu_s^2 = A(T - T_0)$ (Cochran law), where A is a constant and T_0 the transition temperature. This behavior is equivalent to the Curie-Weiss law ($\epsilon(0) = C/(T - T_0)$), which describes the anomaly in the temperature dependence of the static dielectric constant. The situation in CaTiO_3 is more complicated because several modes takes part in softening process. The softening of the lowest-frequency mode stops at 66 cm^{-1} . In Fig 6, we show the plot of ν_T^2 vs. T for several phonons. The soft mode frequency in this plot can be fit approximately by a straight line given by the formula $\nu_T^2 = 27 \times (T + 105) \text{ cm}^{-2}$, which intersects the T -axis at a negative value $T_0 \approx -105 \text{ K}$. The negative Curie temperature confirms that CaTiO_3 behaves as an incipient ferroelectric, as was previously deduced from dielectric data[26]. The behavior of CTO, however, contrasts with that of the well-known incipient ferroelectric SrTiO_3 , where the extrapolated T_c is *positive*[40]. In the case of SrTiO_3 , quantum zero-point motion prevents a phase transition; SrTiO_3 is thus a quantum paraelectric. Temperature-dependence of the soft mode frequency characteristic of a quantum paraelectric phase has been observed in the infrared[41] and hyper-Raman[42] spectra of

SrTiO₃.

D Raman spectroscopy

We also measured the unpolarized Raman scattering in back-scattering geometry of both CaTiO₃ ceramics and single crystal samples. Fig 7(a) shows the temperature dependence of Raman spectra for ceramic samples in the broad spectral range between 0 and 1000 cm⁻¹. The room-temperature spectra are in good agreement with the data given in literature[32–34]. They are dominated by two broad bands (150-600 cm⁻¹ and 650-850 cm⁻¹). In addition, sharp features are superimposed on the lower-frequency band. The sharp peaks have been assigned[33] to first order-Raman bands and the broad ones to second-order scattering. This distinction is based on similarity of the spectra CTO and SrTiO₃. In this comparison, the broad bands of CTO correspond to the second-order bands of the cubic phase of SrTiO₃. The sharp first-order Raman peaks of orthorhombic CTO are similar to the first-order Raman peaks of tetragonal SrTiO₃, which appear below 110 K. On cooling the relative intensity of the broad bands decreases and some additional sharp peaks appear. The anomalous temperature softening of several overtones probably arises from the T -dependence of the soft mode. Among various phonon lines, we focus here on the low-frequency one at 112 cm⁻¹, which is observed in the Raman spectra of ceramics at T=290 K [Fig 7(b)]. The frequency of this line softens to 80 cm⁻¹ at T=10 K, in reasonable agreement with the temperature-dependent frequency of the IR-active soft mode. In contrast to the Raman spectra of ceramics, this additional line can barely be seen in the Raman spectrum of the high quality crystal, as demonstrated in Fig 7(b).

Symmetry analysis shows that the soft mode in orthorhombic CTO is not Raman active to first order. This mode is nonetheless observable in the Raman spectra, probably due to perturbation of the perfect crystal symmetry by grain boundaries in ceramics[43] or to second order processes both in ceramics and single crystals. This work reports a Raman signature for the soft mode in CTO for the first time.

E Comparison with first principles results

First-principles results provide a basis for more detailed interpretation of the observed phonon spectra than has previously been possible. Cockayne and Burton[2] calculated the phonon spectra for the Γ , X, M, and R points of cubic CaTiO_3 and for the zone center of orthorhombic CaTiO_3 . They used density functional theory and Vanderbilt-type ultrasoft pseudopotentials[44], as coded in the package VASP[45–48].

The phonon calculations for cubic CTO were done via the frozen phonon method on a 20-atom supercell equivalent to the primitive cell of the orthorhombic structure. This allows one to estimate the phonon frequencies of intermediate orthorhombic structures via interpolation. Given the 60×60 dynamical matrices for the cubic and orthorhombic calculations D_{cubic} and D_{ortho} , one obtains interpolated phonon frequencies by finding the eigenvalues of $D(\lambda) \equiv (1 - \lambda)D_{\text{cubic}} + \lambda D_{\text{ortho}}$. The infrared-active normal mode frequencies as a function of λ are shown in Figure 2.

Figure 2 is useful for several reasons. It provides a clear graphical representation of the symmetry relationship between orthorhombic modes and corresponding cubic ones. It allows convenient description of orthorhombic phonon eigenvectors in terms of the corresponding cubic ones. The relatively large shifts of phonon frequencies between $\lambda = 0$ and $\lambda = 1$ (and the significant mixing of eigenvector that we find in some cases) calls into question the assumption that the orthorhombic phase is a small perturbation of the cubic one. Finally, the graph allows estimates of the temperature dependence of phonon frequencies of orthorhombic CTO. As λ increases, octahedral tilting and orthorhombic distortion of the cell increases, mimicking the effect of decreasing temperature. In particular, the λ -dependence of frequencies in Figure 2 can be used to identify the soft modes.

Table V compares the low-temperature experimental and first-principles (FP) results. The phonon frequencies agree well, except that the FP frequencies are generally 10 to 20 cm^{-1} lower than the experimental ones, a discrepancy which increases with increasing frequency. These differences are most likely a result of errors in the density functional theory calculations arising from the local density approximation (LDA). (The LDA is well

known to underestimate lattice parameters. We used the experimental lattice parameters for CTO here, based on previous calculations showing much better results for the static dielectric constant of CTO if one uses the experimental lattice parameters rather than the LDA ones[2].) experimental lattice parameters were used in the calculations.) There is also good agreement between the relative oscillator strengths predicted from FP and those observed. Quantitative agreement of oscillator strengths is very good for $\nu > 400 \text{ cm}^{-1}$ but only fair for lower frequencies. The calculated mean of the electronic dielectric tensor ϵ_∞ , is 6.08. The fits to our experimental data give the practically temperature-independent value $\epsilon_\infty = 5.7$. Our results are consistent with the well-known tendency of density functional calculations within the local density approximation to slightly overestimate ϵ_∞ [49].

In the following, we interpret the observed phonon spectra of CTO. First, we identify the bands most closely associated with cubic F_{1u} modes, then we identify the interband features. We give the experimental frequencies at 6 K, and label modes according to the FP results (Table V and Figure 2).

68 cm^{-1} to 124 cm^{-1} : In this frequency range, there is a $1 B_{1u} + 1 B_{2u} + 1 B_{3u}$ pseudotriplet of modes with very high oscillator strengths. The eigenvectors are cubic $1 \Gamma F_{1u}$ -like and are a superposition of a Ca-TiO₃ lattice mode and O-Ti-O bending, with Ca and Ti moving in the same direction. These modes are difficult to individually resolve by reflectivity data because $R \approx 1$, and because of the directional averaging of reflectance. The strong softening as temperature decreases is consistent with the decreases in ν with increasing λ in Figure 2. It is possible that the $1 B_{2u}$ mode contributes to the high oscillator strength of the 124 cm^{-1} feature at 6 K, although Figure 6 shows that this mode hardens to $\nu = 140 \text{ cm}^{-1}$ at $T=300 \text{ K}$, where its oscillator strength is much too small for it to be the $1 B_{2u}$ mode.

224 cm^{-1} to 260 cm^{-1} : As seen in Figure 2, the cubic $2 \Gamma F_{1u}$ triplet splits to an orthorhombic $4 B_{1u} + 3 B_{2u} + 3 B_{3u}$ pseudotriplet in the 200 cm^{-1} to 260 cm^{-1} range in the orthorhombic phase. Calculations show significant mixing with other modes. As with the first pseudotriplet, the eigenvectors are a mix of the Ca-TiO₃ lattice mode and O-Ti-O bending, but now Ca and Ti move out-of-phase. The effective charges of the cations moving in opposite directions largely cancel, leading to phonons whose oscillator strengths

are relatively small. The $3 B_{2u}$ and $4 B_{1u}$ components are resolved experimentally at 224 cm^{-1} and 260 cm^{-1} , respectively. It is puzzling that no mode can be so clearly identified as the $3 B_{3u}$ component of this pseudotriplet (predicted $\nu \approx 199 \text{ cm}^{-1}$).

495 cm^{-1} to 549 cm^{-1} : The mode observed at 549 cm^{-1} is clearly identified as a $7 B_{1u} + 8 B_{2u} + 9 B_{3u}$ pseudotriplet related to the $3 \Gamma F_{1u}$ cubic perovskite B-O-B stretching mode. The $8 B_{2u}$ component is close enough in frequency to the $7 B_{2u}$ component of the 495 cm^{-1} pseudodoublet to transfer some oscillator strength to it.

124 cm^{-1} to 181 cm^{-1} : This is the most interesting region. Despite the relatively high oscillator strengths of the modes in this region, they arise not from cubic F_{1u} modes, but from cubic zone-boundary features. Two distinct B_{1u} modes which are cubic X E_g -like appear in this region and are predicted to show significant softening (Figure 2). For this reason, we identify the mode that softens from 140 cm^{-1} to 110 cm^{-1} as the $2 B_{1u}$ mode and the mode that softens from 180 cm^{-1} to 170 cm^{-1} as the $3 B_{1u}$ mode. These modes are primarily O-Ti-O bending modes, except that the Ti in alternating planes move largely out of phase. Octahedral tilting makes these modes polar in the orthorhombic phase. Note that all modes that show significant softening involve O-Ti-O bending; thus the soft mode behavior in CaTiO_3 is mainly due to changes in Ti-O bonding as octahedra tilting angles and Ti-O distances change with temperature. In addition to the X E_g -like modes, computations show a $2 B_{2u} + 2 B_{3u}$ pseudodoublet at around 160 cm^{-1} to 170 cm^{-1} which arises the cubic 1 M E_u doublet. This pseudodoublet is primarily a Ca mode, in which different Ca move largely out of phase. The assignment in Table V of this doublet to two distinguishable modes is uncertain. Remarkably, since the modes in this region have higher oscillator strengths than those in the second F_{1u} band, one obtains their frequencies ($\approx 160 \text{ cm}^{-1}$) in fitting to a pseudocubic model, rather than the the average frequency of the real $2 \Gamma F_{1u}$ band ($\approx 220 \text{ cm}^{-1}$ [3]).

$261\text{-}495 \text{ cm}^{-1}$: The phonons in this region are easily and clearly identified in the first principles calculations. Most significant is a $5 B_{1u} + 7 B_{3u}$ pseudodoublet at 435.5 cm^{-1} which arises from a $R F_{2g}$ phonon that becomes polar under octahedral tilting as shown in Figure 8. Note that this feature was misidentified as a component of the $3 \Gamma F_{1u}$ -like

pseudotriplet in an early study on CTO[29]. The next strongest modes, at 305 cm^{-1} and 322 cm^{-1} , have eigenvectors similar to cubic X modes with most ionic motion in the z direction and with opposite motion of atoms in successive layers in the z direction. The 5 B_{2u} mode at 305 cm^{-1} is dominated by oxygen and Ti moving in the same direction within a layer. The 5 B_{3u} mode at 322 cm^{-1} has a torsional oxygen vibration pattern within a layer. Both these modes become polar due to octahedral tilting.

Above 549 cm^{-1} : The 645 cm^{-1} feature seen clearly in the reflectivity data is a puzzle since no TO phonons are calculated to have such high frequencies. It is possible that this feature corresponds to a localized mode arising from tilting domain boundaries.

V. CONCLUSION

We have used spectroscopic techniques to study temperature dependence of infrared and Raman spectra of CaTiO_3 . We have analyzed the infrared spectra by different fitting procedures, thereby determining phonon frequencies and dielectric dispersion. Three modes soften significantly (shift to lower frequency) with decreasing temperature. Their temperature behavior accounts for characteristics of an incipient ferroelectric, in agreement with earlier dielectric studies. Using first-principles calculations, we identified the symmetries and phonon eigenvectors of nearly all of the observed modes, including those associated with zone-boundary phonons of the cubic perovskite phase. We have observed for the first time the soft mode in the Raman spectra of ceramic samples.

VI. ACKNOWLEDGEMENTS

This work has been supported by the Grant Agency of the Acad. Sci. CR under Contract No. A1010918 and the Grant Agency of the Czech Rep. under Contract No. 202/01/0612. We would like to thank B.T. Melekh (A.F. Ioffe Institute) for the growth of the CaTiO_3 single crystals. At A.F. Ioffe Institute this work was partly supported by the NWO grant.

VII. APPENDIX

In this Appendix, we give expressions for the directional dependence of the dielectric function in an anisotropic crystal and discuss the implications of directional averaging on model fitting.

The dielectric function for an anisotropic crystal is actually a second rank tensor $\overleftrightarrow{\epsilon}(\nu)$. In principle, one can determine the complete tensor by a set of reflectivity measurements on a single crystal, using polarized light whose electric field has different orientations \hat{n} relative to the crystal axes. For each polarization direction, one measures the dielectric function for that direction: $\epsilon(\nu, \hat{n}) \equiv \hat{n} \cdot \overleftrightarrow{\epsilon}(\nu) \cdot \hat{n}$. Then, $\epsilon_{\alpha\alpha}(\nu) = \epsilon(\nu, \hat{\alpha})$ and $\epsilon_{\alpha\beta}(\nu) = \epsilon(\nu, (\hat{\alpha} + \hat{\beta})/\sqrt{2}) - \epsilon_{\alpha\alpha}(\nu)/2 - \epsilon_{\beta\beta}(\nu)/2$.

The above expressions are exact. In the remainder of this Appendix, we assume that the dielectric function can be physically described by a damped oscillator model, and generalize Eqs. IV.1 and IV.2 to properly include direction dependence. In the three-parameter model,

$$\epsilon(\nu, \hat{n}) = \hat{n} \cdot \overleftrightarrow{\epsilon}_{\infty} \cdot \hat{n} + \sum_i \frac{3\Delta\epsilon_i(\hat{n} \cdot \hat{p})^2\nu_{iLO}^2}{\nu_{iTO}^2 - \nu^2 + i\gamma_{iTO}\nu}, \quad (\text{VII.1})$$

where \hat{p} is the electric polarization direction of the i -th phonon. Likewise, in the four-parameter model:

$$\epsilon(\nu, \hat{n}) = (\hat{n} \cdot \overleftrightarrow{\epsilon}_{\infty} \cdot \hat{n}) \prod_i \frac{\nu_{iLO}^2(\hat{n}) - \nu^2 + i\gamma_{iLO}(\hat{n})\nu}{\nu_{iTO}^2 - \nu^2 + i\gamma_{iTO}\nu} \quad (\text{VII.2})$$

where the LO frequencies and damping terms are now direction-dependent.

The above expressions allow one to fit the dielectric function of a single crystal as a function of ν and \hat{n} and thus derive the full dielectric tensor, as was done for trigonal rare-earth chlorides by Berreman and Unterwald[37]. Unfortunately, we are unable to do this for the CTO samples in the present work. For the ceramic samples, different grains have different orientations \hat{n} with respect to the electric field polarization of the incident light, even if polarized light is used. In our single crystal samples, there are tilting domains, therefore \hat{n} is different for different domains. Given that directional information of the dielectric function is already lost, unpolarized light was used in this work. To properly analyze the reflectivity results, one must derive the proper reflectivity expressions for a

multigrain and/or multidomain anisotropic crystal. This result will depend on the details of the microstructure. In the case of CTO, we assume that inhomogeneities due to domain boundaries are small and that we can neglect depolarizing fields. This is justified when one has a single phase sample with small anisotropy of the dielectric function. In the following, we analyze in terms of two simplified models: first an effective permittivity model and secondly an average reflectivity model.

In the effective permittivity model, the inhomogeneities are averaged out such that the incident light sees a homogeneous medium whose dielectric function is the the direction-averaged dielectric function of the underlying crystal. Thus $\epsilon_{eff}(\nu) = (1/(4\pi)) \int d\hat{n} \epsilon(\nu, \hat{n})$.

In this model,

$$R_{eff}(\nu) = \left| \frac{\sqrt{\epsilon_{eff}(\nu)} - 1}{\sqrt{\epsilon_{eff}(\nu)} + 1} \right|^2. \quad (\text{VII.3})$$

Because $\vec{\epsilon}$ is a second rank tensor, $\epsilon_{eff}(\nu) = \text{Tr}(\vec{\epsilon}(\nu))/3$. For the three-parameter oscillator model VII.1, we reobtain Eq. IV.1, with $\epsilon_\infty = \text{Tr}(\vec{\epsilon}_\infty)/3$. In other words, fitting $\epsilon_{eff}(\nu)$ via a three parameter model gives the correct physical values for ϵ_∞ , ν_{TOi} , $\Delta\epsilon_i$, and γ_{TOi} , even though the crystal is anisotropic. Only the phonon polarization directions \hat{p}_i are undetermined. Similarly, neglecting damping, the directional averaging of the four-parameter model VII.2 can be expressed in the form of Eq. IV.2, which yields the correct physical values for ϵ_∞ , ν_{TOi} , and $\Delta\epsilon_i$, (the LO frequencies determined are the zeroes of $\epsilon_{eff}(\nu)$ and do not represent the set of LO frequencies for any particular direction \hat{n}). Assuming that the directional dependence of $\gamma_{iLO}(\hat{n})$ is small, the 4-parameter model will yield physically meaningful parameters even in the presence of damping.

Things are more complicated, however, if one averages reflectances rather than dielectric functions. Suppose that different regions of the surface reflect incident radiation according to the local \hat{n} , without constructive or destructive interference. Then, the total reflectivity is the average of reflectance over directions $R_{ave}(\nu) = (1/(4\pi)) \int d\hat{n} R(\nu, \hat{n})$. Given the nonlinear relationship between R and $\epsilon(\nu)$ (IV.4), however, $R_{ave}(\nu)$ is *not* equal to $R_{eff}(\nu)$. In this case, the physical validity of the parameters obtained by model fitting comes into question.

It is difficult to derive analytical results for the relationship between the oscillator pa-

rameters determined from fitting $R_{ave}(\nu)$ to a particular model and those of the original oscillator model. To gain insight into the issues involved, we selected a specific model for CTO and compared the reflectivities derived under effective permittivity theory with the average reflectivity. For simplicity, we used a three-parameter model, with ϵ_∞ , ν_{TOi} , and $\Delta\epsilon_i$ taken from Ref.[2], and with the same damping parameter 20 cm^{-1} for all modes. Results are shown in Figure 9. Fortunately, the two results are very similar for most frequencies. The largest differences are in the sharp minima of R , especially those near 410 cm^{-1} and 470 cm^{-1} .

Least-squares fits to R_{ave} using the original oscillator parameters as a starting point gives ϵ_∞ correct to within 0.1 % and TO and LO phonon frequencies that are correct to within 1 cm^{-1} , except in the 410 cm^{-1} to 470 cm^{-1} region, where errors as large as 3 cm^{-1} occur. On the other hand, some damping terms in the highly dispersive region have errors that are greater than a factor of 2. The oscillator strengths for isolated modes with strength greater than 0.1 are correct to within 30 %; the weakest modes and individual modes in pseudomultiplets have larger relative errors, though the combined oscillator strength of each pseudomultiplet is correct to within 30 %.

This Appendix shows the significance of directional averaging for a ceramic or multidomain single crystal in interpreting the parameters obtained in a reflectivity fit. We suspect that the observed reflectance in our experiments on single crystal CTO is between R_{eff} and R_{ave} , but closer to R_{ave} . We conclude that the frequencies determined in the fits are highly reliable and that the oscillator strengths of isolated modes and the combined oscillator strengths of pseudomultiplets are reliable to within 30%. The damping terms, however, are not reliable. Accurate partitioning of oscillator parameters between components of multiplets, and accurate determination of damping parameters will require experiments on single-domain single crystals.

REFERENCES

- [1] D. Vanderbilt, *J. Korean Phys. Soc.* **32**, S103 (1998).

- [2] E. Cockayne and B.P. Burton, *Phys. Rev. B* **62**, 3735 (2000).
- [3] E. Cockayne, *J. Appl. Phys.* **90**, 1459 (2001).
- [4] R.D. King-Smith and D. Vanderbilt, *Phys. Rev. B* **49**, 5828 (1994).
- [5] W. Zhong, R.D. King-Smith, and D. Vanderbilt, *Phys. Rev. Lett.* **72**, 3618 (1994).
- [6] W. Zhong and D. Vanderbilt, *Phys. Rev. Lett.* **74**, 2587 (1995).
- [7] Ph. Ghosez, E. Cockayne, U.V. Waghmare, and K.M. Rabe, *Phys. Rev. B* **60**, 836 (1999).
- [8] D. Vanderbilt and W. Zhong, *Ferroelectrics* **206,207**, 181 (1998).
- [9] H.F. Kay and P.C. Bailey, *Acta Cryst.* **10**, 219 (1957).
- [10] A.R. Chakhmouradian and R.H. Mitchell, *J. Sol. St. Chem.* **138**, 272 (1998).
- [11] C.J. Ball, B.D. Begg, D.J. Cookson, G.J. Thorogood, and E.R. Vance, *J. Sol. St. Chem.* **139**, 238 (1998).
- [12] R. Ranjan and D. Pandey, *J. Phys.: Condens. Matter* **11**, 2247 (1999).
- [13] R. Ranjan and D. Pandey, *J. Phys.: Condens. Matter* **13**, 4251 (2001).
- [14] H. F. Naylor and O. A. Cook, *J. Am. Chem. Soc.* **68**, 1003 (1946).
- [15] B.J. Kennedy, C.J. Howard, and B.C. Chakoumakos, *J. Phys.: Condens. Matter* **11**, 1479 (1999).
- [16] T. Vogt and W.W. Schmahl, *Europhys. Lett.* **24**, 281 (1993).
- [17] S.A. Redfern, *J. Phys.: Condens. Matter* **8**, 8267 (1996).
- [18] T. Matsui, H. Shigematsu, Y. Arita, Y. Hanajiri, N. Nakamitsu, T. Nagasaki, *J. Nuclear Mat.* **247**, 72 (1997).
- [19] A.M. Glazer, *Acta Cryst.* **B 28**, 3384 (1972).
- [20] A.M. Glazer, *Acta Cryst.* **A 31**, 751 (1975).
- [21] P.M. Woodward, *Acta Cryst.* **B 53**, 32 (1997).
- [22] C.J. Howard and H.T. Stokes, *Acta Cryst.* **B 54**, 752 (1998).
- [23] S. Kucheiko, J.-W. Choi, H.-J. Kim, and H.-J. Jung, *J. Am. Ceram. Soc.* **79**, 2739 (1996).
- [24] T. Nakamura, P.-H. Sun, Y.J. Shan, Y. Inaguma, M. Itoh, I.-S. Kim, J.-H. Sohn, M. Ikeda, T. Kitamura, H. Konagaya, *Ferroelectrics* **196**, 205 (1997).

- [25] J. Petzelt, S. Pačesová, J. Fousek, S. Kamba, V. Železný, V. Koukal, J. Schwarzbach, B.P. Gorschunov, G.V. Kozlov, A.A. Volkov, *Ferroelectrics* **93**, 77 (1989).
- [26] V.V. Lemanov, A.V. Sotnikov, E.P. Smirnova, M. Weihnacht, R. Kunze, *Sol. St. Comm.* **110**, 611 (1999).
- [27] A. Linz, Jr., and K Herrington, *J. Chem. Phys.* **28**, 824 (1958).
- [28] G. Rupprecht and R.O Bell, *Phys. Rev.* **135**, A 748 (1965).
- [29] C.H. Perry, B.N. Khanna, and G. Rupprecht, *Phys. Rev.* **135**, A 408 (1964).
- [30] C.M. Perry, D.J. McCarthy, and G. Rupprecht, *Phys. Rev.* **138**, A1537 (1965).
- [31] A.S. Knyazev, Yu.M. Poplavko, B.P. Zakharov, and V.V. Alekseev, *Solid State Physics* (Russia) **15**, 3006 (1973).
- [32] P. Gillet, F. Gutytot, G.D. Price, B. Tournerie, and A. Le Cleach, *Phys. Chem. Minerals* **20**, 159 (1993).
- [33] P. McMillan and Nancy Ross, *Phys. Chem. Minerals* **16**, 21 (1988).
- [34] P. Gillet, G. Fiquet, I. Daniel and B. Reynard, *Geophysical Research Letters* **20**, 1931 (1993).
- [35] U. Balachandran and N.C. Eror, *Sol. St. Comm.* **44**, 815 (1982).
- [36] Disclaimer: Certain commercial equipment, instruments, or materials are identified in this paper to specify the experimental procedures adequately. Such identification is not intended to imply recommendation or endorsement by the National Institute of Standards and Technology, nor is it intended to imply that the materials or equipment identified are necessarily the best available for the purpose.
- [37] D.W. Berreman and F.C. Unterwald, *Phys. Rev.* **174** 791 (1968).
- [38] F. Gervais, in *Infrared and Millimeter Waves*, vol.8, ed. K.J. Button, 280 (1983).
- [39] M.B. Smirnov, A.P. Mirgorodsky, and P.E. Quintard, *J. Mol. Struct.* **348**, 159 (1995).
- [40] K.A. Müller and H. Burkard, *Phys. Rev. B* **19**, 3593 (1979).
- [41] I. Fedorov, V. Železný, J. Petzelt, V. Trepakov, M. Jelínek, M. Čerňanský, and V. Studnička, *Ferroelectrics* **208-209**, 413 (1998).
- [42] A. Yamanaka, M. Kataoka, Y. Inaba, K. Inoue, and E. Courtens, *Europhys. Lett.* **50**, 688 (2000).

- [43] J. Petzelt *et al.* *Phys. Rev. B* **64**, 184111 (2001).
- [44] D. Vanderbilt, *Phys. Rev. B* **41**, 7892 (1990).
- [45] G. Kresse and J. Hafner, *Phys. Rev. B* **47**, RC558 (1993).
- [46] G. Kresse, Thesis, Technische Universität Wien, 1993.
- [47] G. Kresse and J. Furthmüller, *Comput. Mat. Sci.* **6**, 15 (1996).
- [48] G. Kresse and J. Furthmüller, *Phys. Rev. B* **54**, 11169 (1996).
- [49] Z. H. Levine and D. C. Allan, *Phys. Rev. Lett.* **63**, 1719 (1989).
- [50] L.P. Bouckaert, R. Smoluchowski, and E. Wigner, *Phys. Rev.* **50**, 58 (1936).

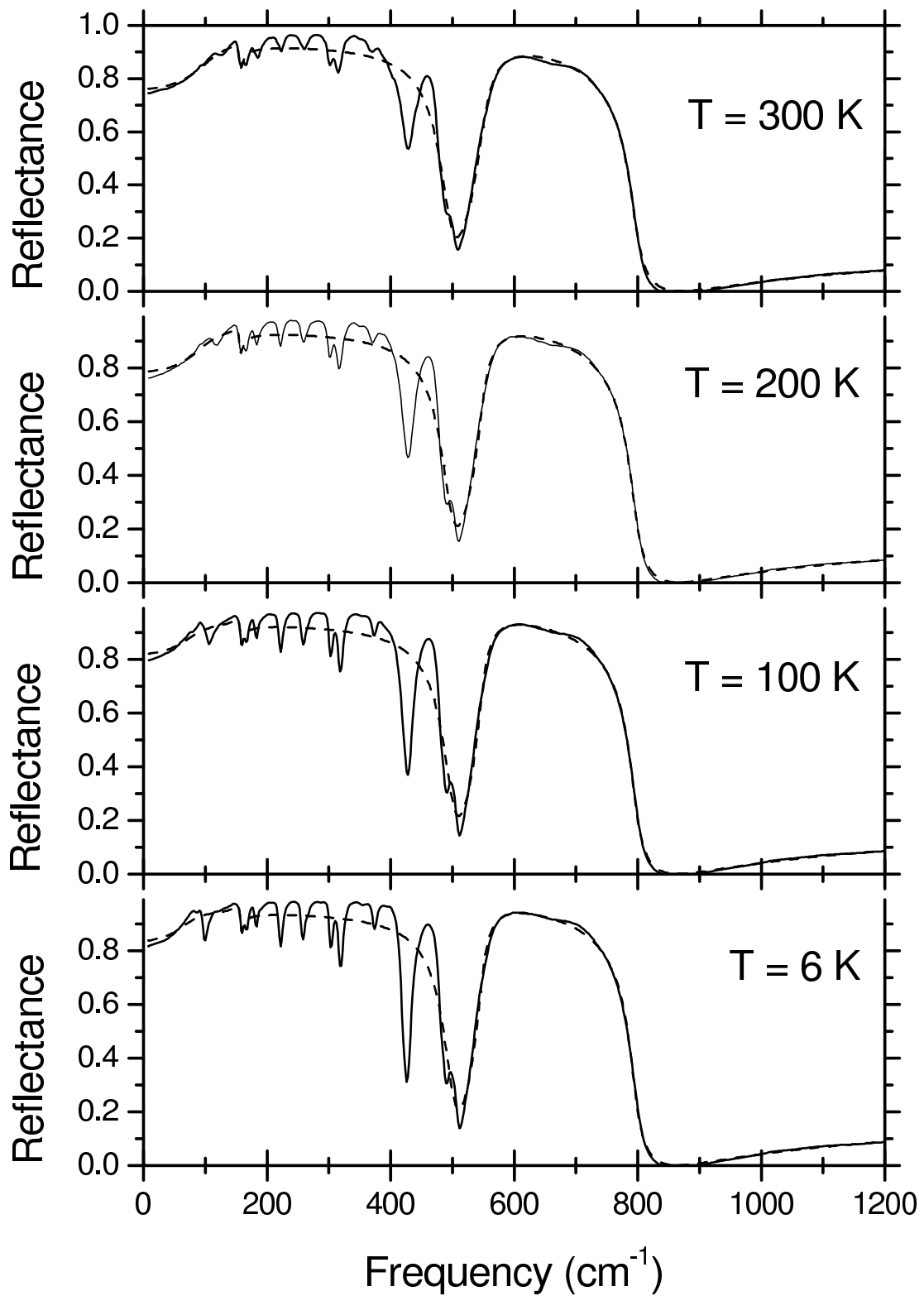


FIG. 1: Frequency dependence of the infrared reflectance for CaTiO_3 at selected temperatures. The experimental data are given by solid lines. The dashed lines represent fits by the 4-parameter model assuming three infrared active modes.

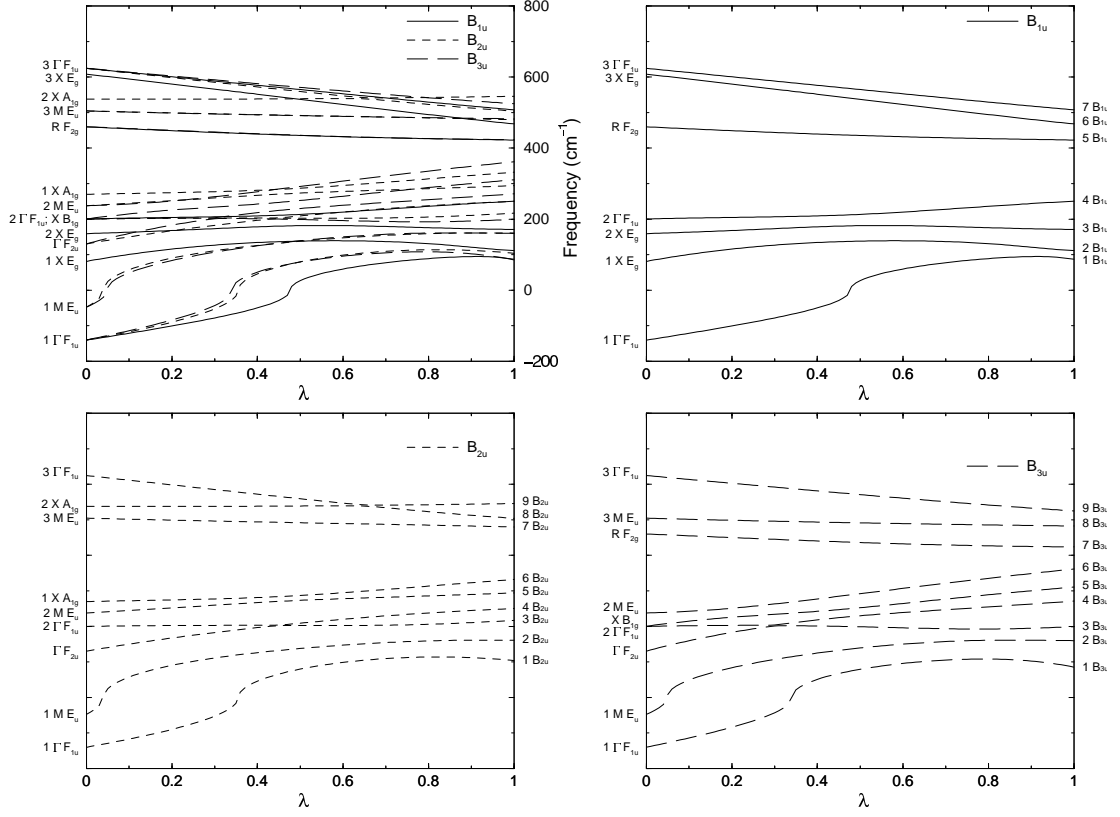


FIG. 2: First-principles frequencies for infrared-active phonons in CaTiO₃. The parameter λ interpolates between results for cubic CaTiO₃ ($\lambda = 0$) and orthorhombic CaTiO₃ ($\lambda = 1$). Although the frequencies are system-dependent, the symmetry relationships between the cubic and orthorhombic modes are general for a Pm3m to Pbnm transition (see also Table II).

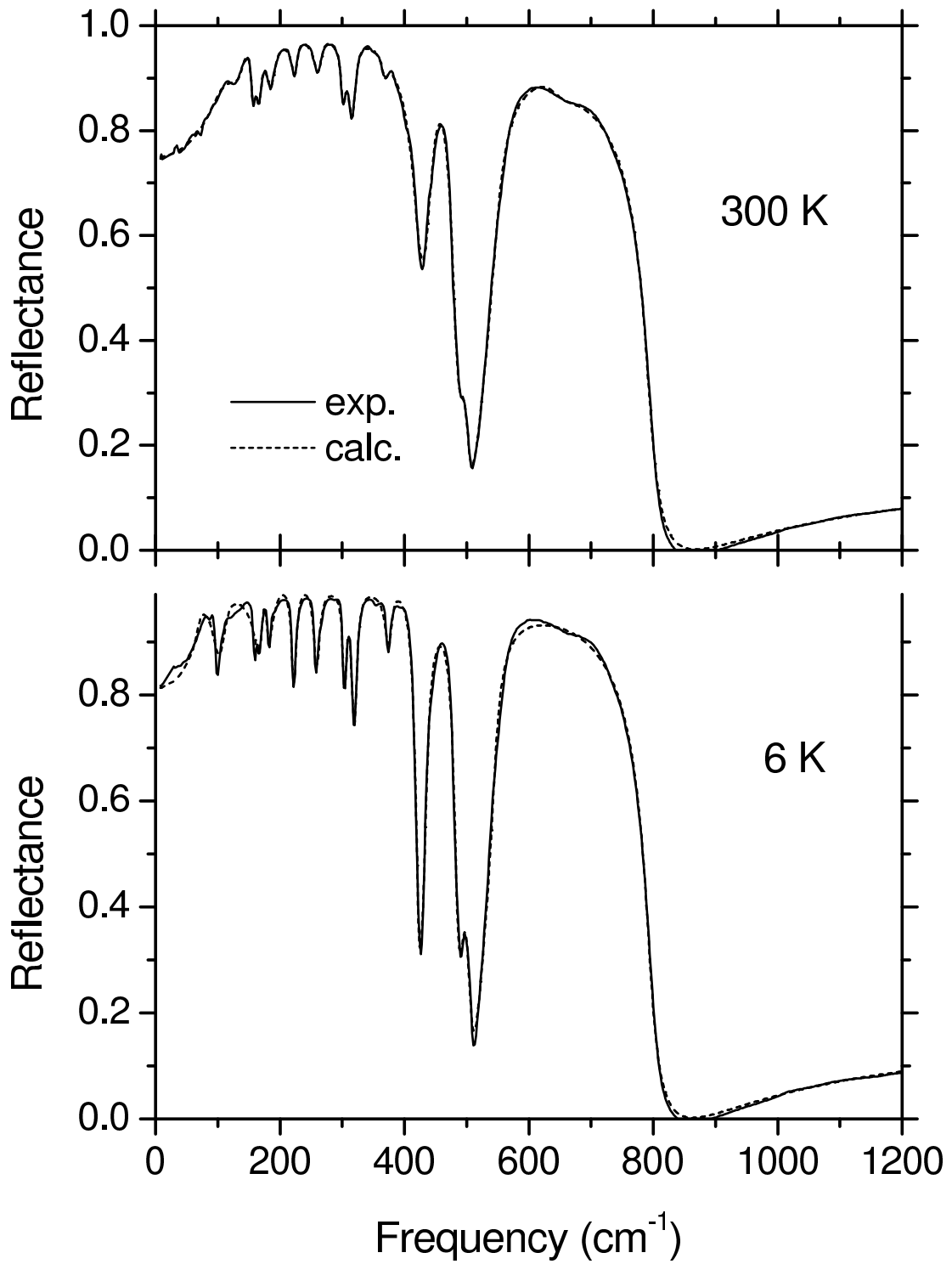


FIG. 3: Infrared reflectance of CaTiO_3 at 6 K and 300 K fitted by the 4-parameter model assuming 14 infrared active modes (optimum fit).

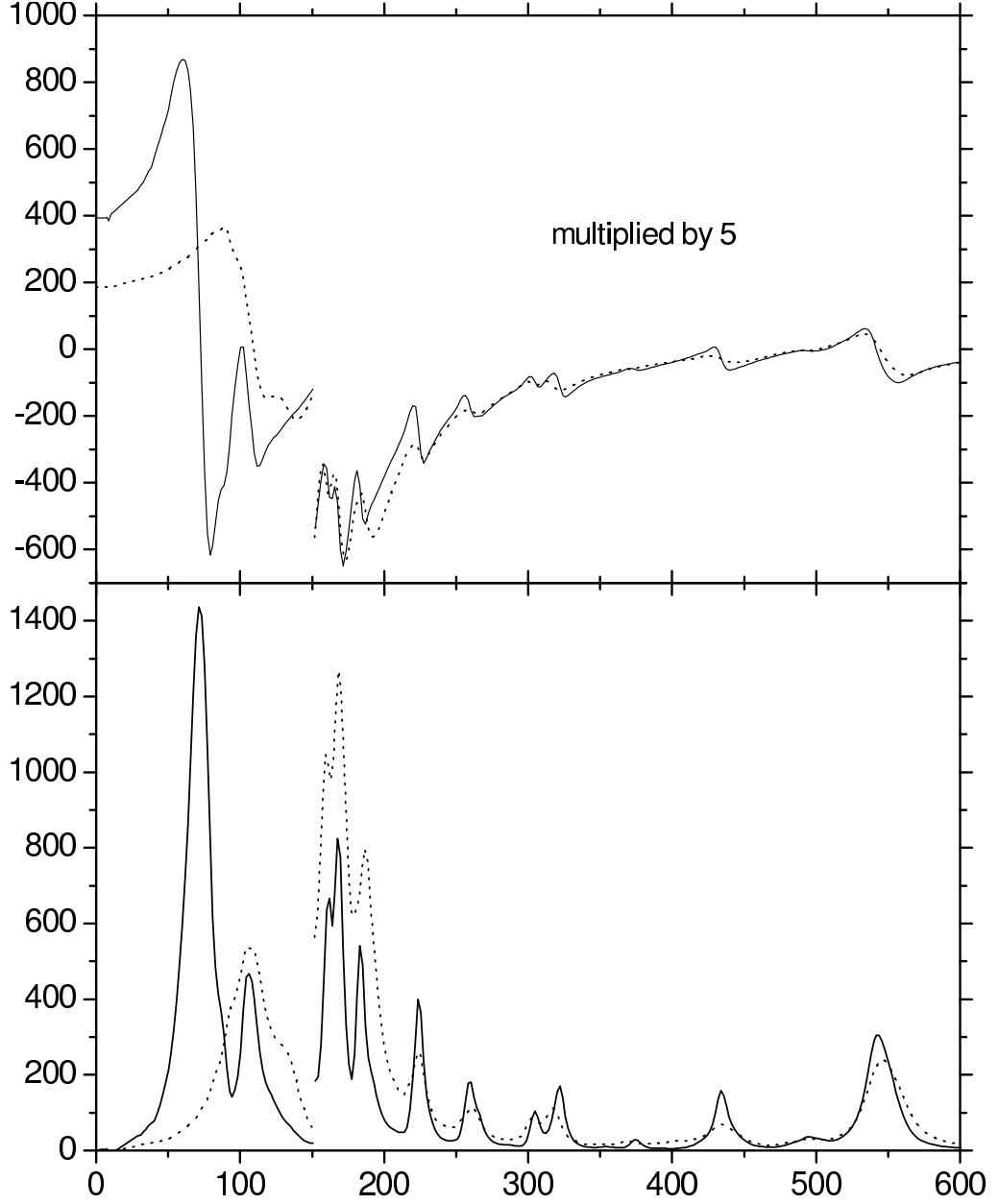


FIG. 4: $\epsilon_1(\nu)$ and $\epsilon_2(\nu)$ for CaTiO_3 at 6 K and 300 K obtained from Kramers-Kronig analysis in the spectral region containing all infrared-active phonons. Pseudocubic modes, as determined from fit to pseudocubic oscillator model, are shown by dark arrows. As discussed in section IV E, however, the modes near 157 cm^{-1} actually arise from cubic zone-boundary modes; the 225 cm^{-1} and 260 cm^{-1} peaks show two components of the second pseudocubic triplet as determined from first-principles calculations.

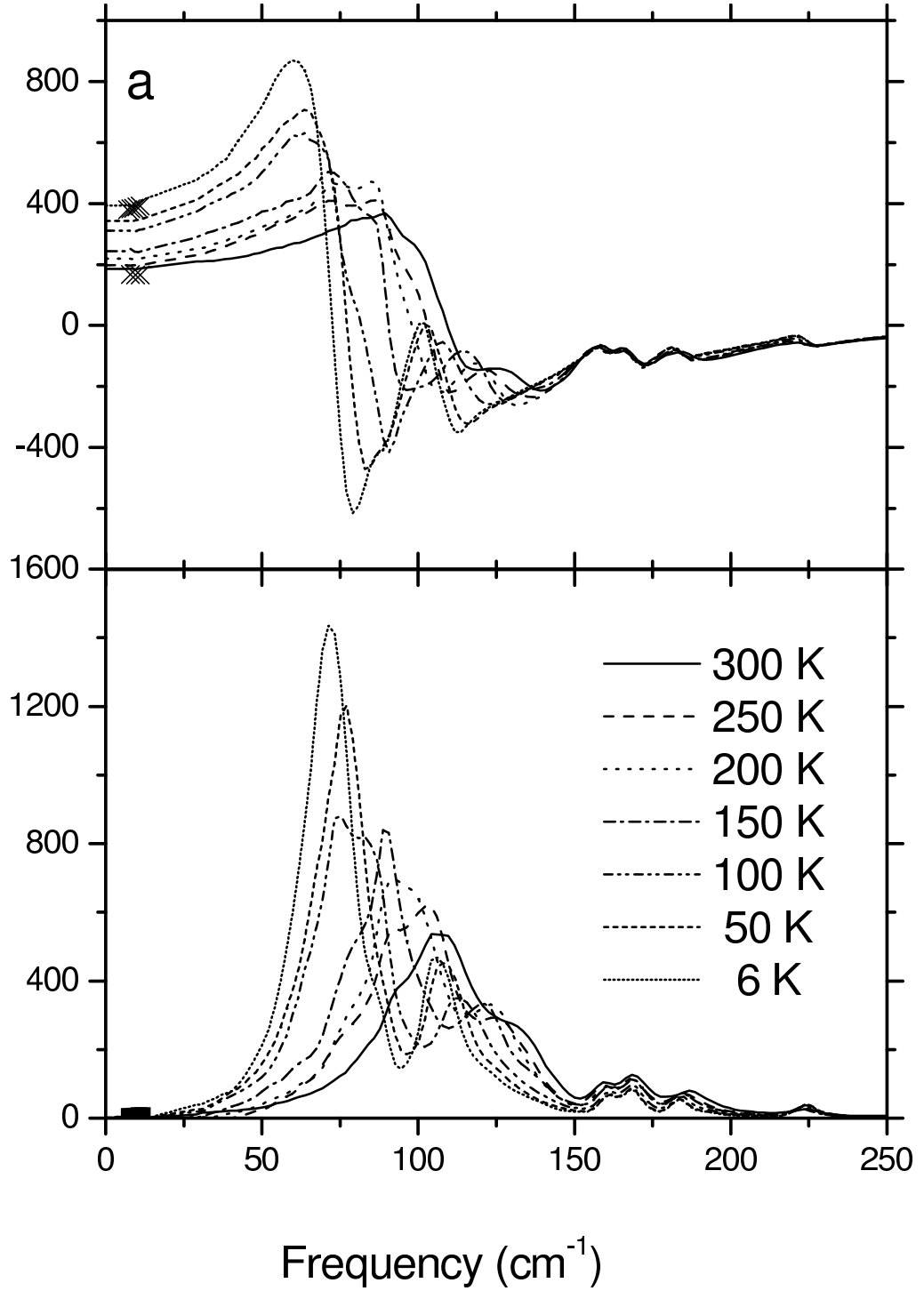


FIG. 5: Temperature dependence of $\epsilon_1(\nu)$ and $\epsilon_2(\nu)$ for CaTiO_3 in the spectral region of the soft modes (below 250 cm^{-1}). Lines are obtained from Kramers-Kronig analysis. Crosses and squares (visible near $\nu = 10 \text{ cm}^{-1}$) are experimental BWO measurements at 6 and 300 K for real and imaginary ϵ , respectively.

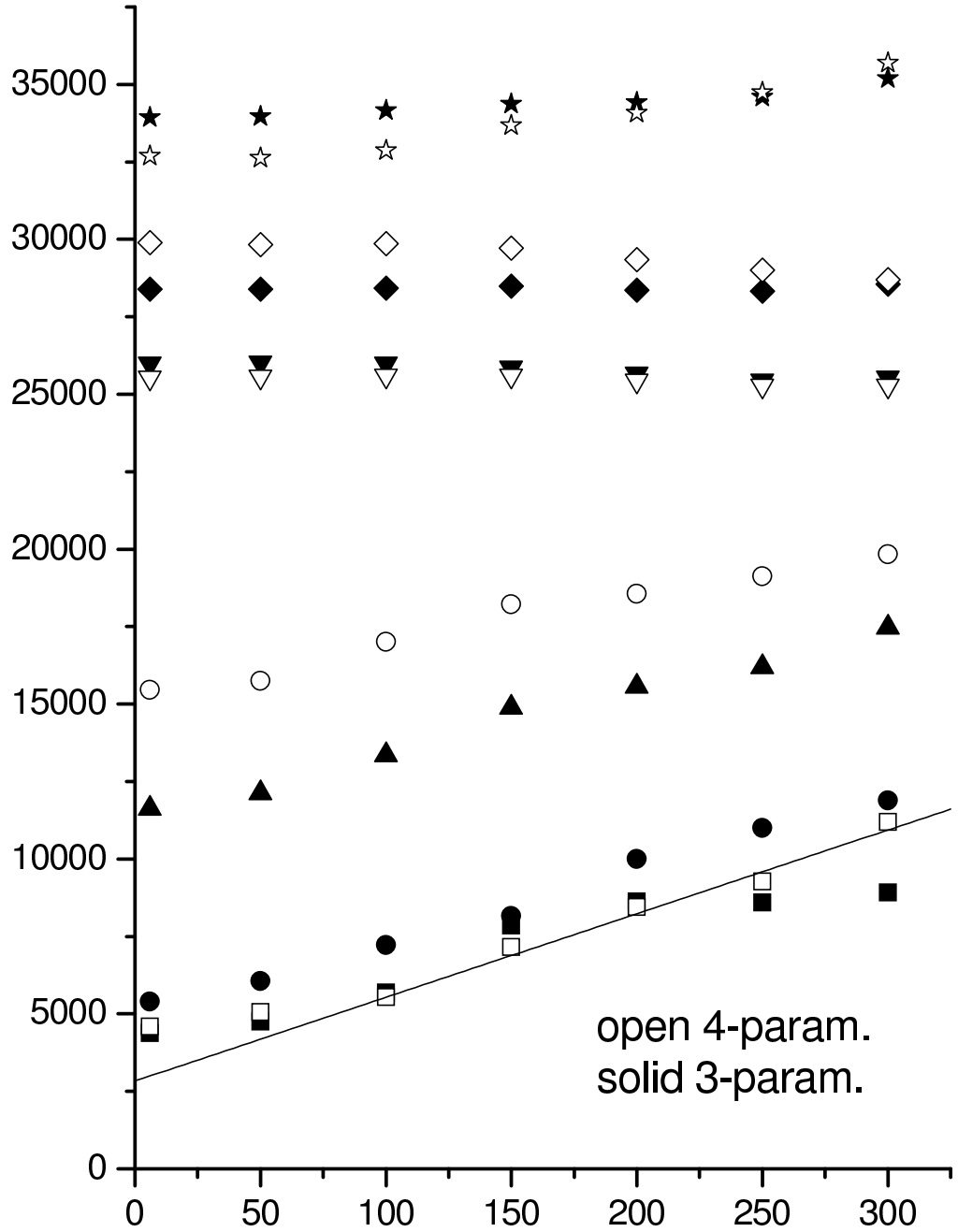


FIG. 6: Temperature dependence of the low-frequency modes. The open symbols were obtained fitting the reflectivity by 4-parameter model assuming 14 modes. The solid symbols results from simultaneously fitting $\epsilon_1(\nu)$ and $\epsilon_2(\nu)$ obtained from K-K analysis. The solid line shows the plot $\nu_T^2 = 27 \times (T + 105)$.

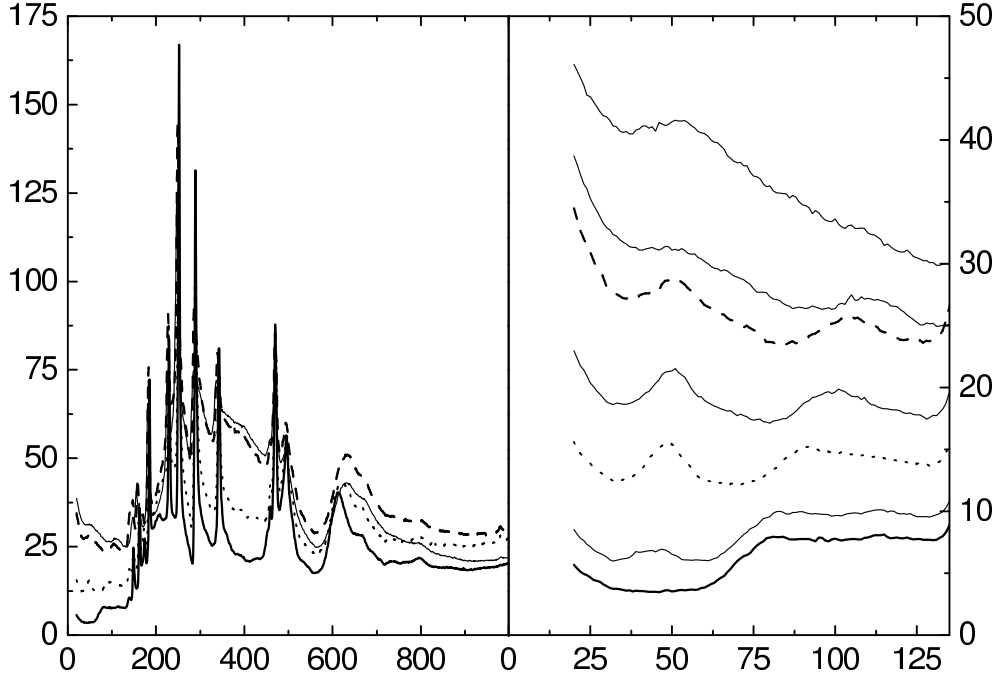


FIG. 7: (a) Temperature-dependent Raman spectra of CaTiO_3 ceramics sample. (b) Low frequency Raman spectra of CaTiO_3 ceramics sample at different temperatures as well as Raman spectrum of CaTiO_3 crystal at room temperature. For clarity, the spectrum marked “290 K crystal” is shifted vertically by 10 units with respect to all the other spectra.

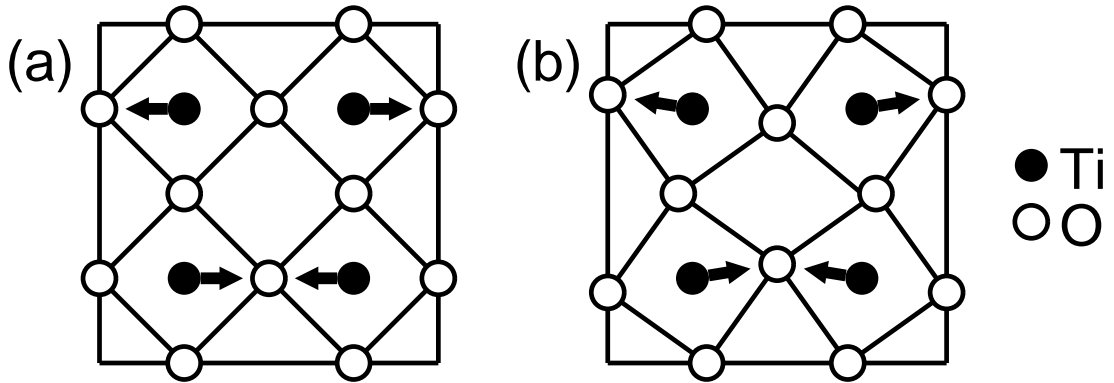


FIG. 8: Schematic of how a zone-boundary phonon for cubic CaTiO_3 (a) can become a polar zone-center mode for orthorhombic CaTiO_3 (b) due to octahedral tilting. The mode shown corresponds to one component of the pseudodoublet observed at $\nu \approx 436 \text{ cm}^{-1}$

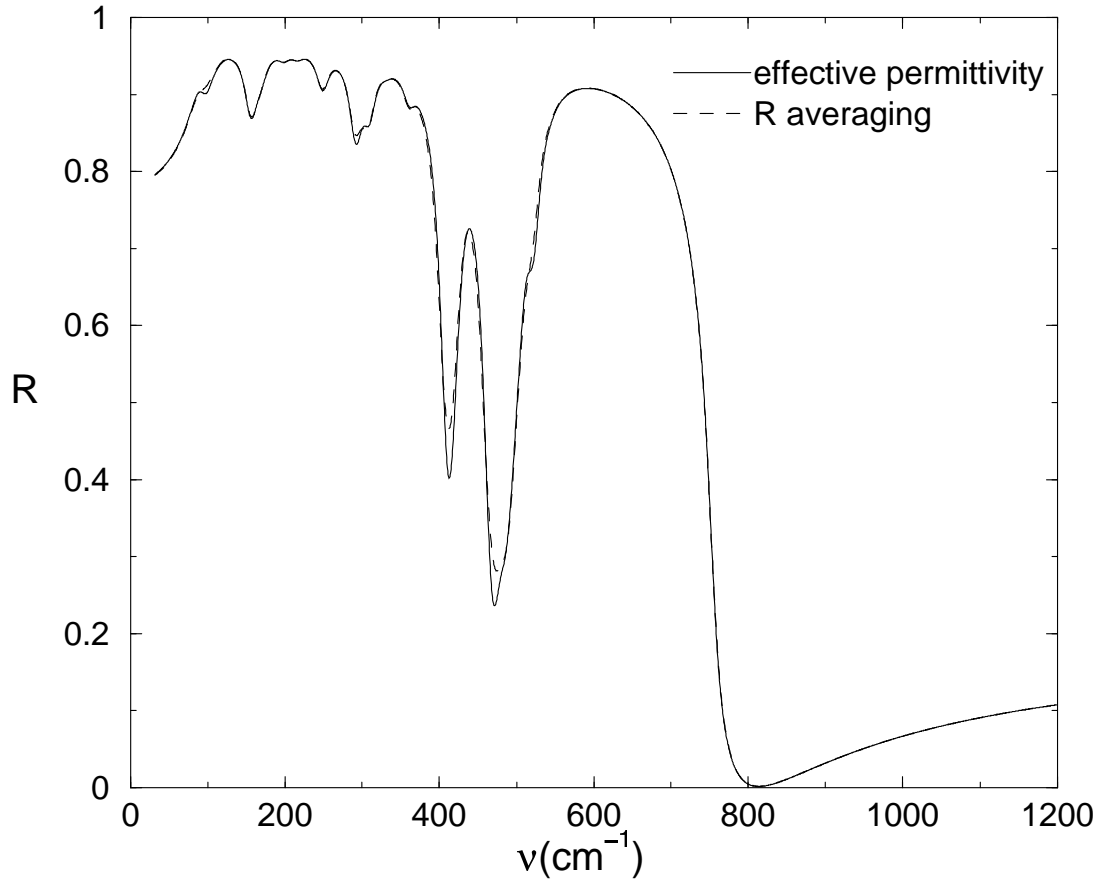


FIG. 9: Comparison of simulated $R(\nu)$ for a CaTiO_3 oscillator model under unpolarized light, based on two different averaging schemes. Note the extreme closeness of the two spectra except in the regions of the sharpest minima.

TABLE I: CaTiO₃ phonon parameters at various temperatures using pseudocubic approximation (3 modes) and fitting to 4-parameter model. ϵ_∞ is 5.6, 5.6, 5.7 and 5.7 for 300, 200, 100 and 6 K, respectively. All frequencies and dampings are in cm^{-1} .

T [K]	ν_T	γ_T	ν_L	γ_L	$\Delta\epsilon$
300	111.5	50.0	155.8	6.0	207.1
	156.9	10.4	496.7	39.3	2.9
	549.4	25.6	793.9	26.5	1.1
200	102.4	46.5	155.7	5.12	267.3
	156.5	9.2	498.3	37.7	1.9
	547.9	46.7	794.2	5.1	1.1
100	85.5	52.1	156.7	4.6	400.9
	157.6	8.1	501.3	37.0	1.2
	547.4	17.9	793.6	22.5	1.0
6	76.9	42.5	157.1	4.6	504.5
	157.6	8.0	501.2	34.6	1.0
	546.8	16.7	793.5	21.7	1.0

TABLE II: Symmetry relationships between phonons for cubic perovskite structure and for $a^-a^-b^+$ tilted Pbmn orthorhombic perovskites. Symmetry labels in Bouckaert *et al.* notation are given for comparison with recent first-principles literature. All orthorhombic modes are zone-center.

Cubic mode (point group notation)	Cubic mode (Bouckaert <i>et al.</i> notation[50])	Orthorhombic mode(s)
ΓF_{1u}	Γ_{15}	$B_{1u} + B_{2u} + B_{3u}$
ΓF_{2u}	Γ_{25}	$A_u + B_{2u} + B_{3u}$
$X A_{1g}$	X_1	B_{2u}
$X A_{2u}$	$X_{2'}$	B_{2g}
$X B_{1g}$	X_3	B_{3u}
$X E_g$	X_5	$A_u + B_{1u}$
$X E_u$	$X_{5'}$	$A_g + B_{1g}$
$M A_{1g}$	M_1	B_{1g}
$M A_{2g}$	M_2	A_g
$M A_{2u}$	$M_{2'}$	A_u
$M B_{1g}$	M_3	A_g
$M B_{1u}$	$M_{3'}$	A_u
$M B_{2g}$	M_4	B_{1g}
$M E_g$	M_5	$B_{2g} + B_{3g}$
$M E_u$	$M_{5'}$	$B_{2u} + B_{3u}$
$R A_{2u}$	$R_{2'}$	B_{3g}
$R E_u$	$R_{12'}$	$B_{2g} + B_{3g}$
$R F_{1u}$	R_{15}	$A_g + B_{1g} + B_{3g}$
$R F_{2g}$	$R_{25'}$	$A_u + B_{1u} + B_{3u}$
$R F_{2u}$	R_{25}	$A_g + B_{1g} + B_{2g}$

TABLE III: CaTiO₃ phonon parameters at various temperatures, using 14 modes and fitting to 4-parameter model. ϵ_∞ is 5.6 and 5.7 for 300 and 6 K, respectively. All frequencies and dampings are in cm⁻¹.

T [K]	ν_T	γ_T	ν_L	γ_L	$\Delta\epsilon$
300	105.8	32.3	139.2	36.7	167.14
	140.8	19.1	156.5	8.0	3.78
	159.0	8.2	165.6	10.7	2.87
	169.4	9.7	183.4	17.7	5.45
	189.0	16.7	223.8	11.6	6.04
	225.4	10.5	261.5	15.1	0.95
	263.1	14.0	300.9	8.2	0.47
	302.0	8.5	315.9	13.7	0.16
	318.5	12.4	368.4	10.9	0.39
	368.8	11.0	426.8	32.2	0.03
	439.7	25.0	483.6	21.2	0.36
	495.3	23.0	503.7	17.0	0.08
	548.6	25.9	644.4	54.6	1.38
	644.9	56.3	795.1	27.1	0.01
6	67.7	13.6	107.1	79.9	295.05
	124.3	39.2	159.1	3.6	42.20
	159.8	3.6	164.4	18.9	0.40
	172.9	12.0	178.7	7.9	7.83
	180.8	18.5	220.7	7.7	4.55
	224.3	9.1	256.9	10.1	1.86
	259.9	11.8	303.1	6.7	0.94
	304.9	6.8	318.1	8.5	0.25
	321.7	9.1	374.8	12.3	0.55
	376.1	11.7	422.1	11.4	0.09
	435.5	12.5	485.2	14.7	0.48
	494.9	18.7	506.8	15.2	0.11
	545.6	16.7	642.2	54.3	1.24
	642.1	55.2	794.5	24.2	0.01

TABLE IV: CaTiO₃ phonon parameters at room temperature and 6 K obtained by fitting simultaneously the low-frequency part of $\epsilon_1(\nu)$ and $\epsilon_2(\nu)$ to a 3-parameter model. All frequencies and dampings are in cm⁻¹.

T [K]	ν_T	$\Delta\epsilon$	γ
300	94.4	46.4	27.1
	109.1	108.3	26.4
	132.2	18.6	16.5
	159.8	1.1	4.1
	168.9	5.2	9.7
	187.6	3.9	13.4
	224.2	0.6	7.5
6	66.2	131.1	17.0
	73.4	210.4	13.5
	107.8	50.6	13.2
	161.2	1.4	5.0
	168.5	2.5	6.2
	184.2	1.4	5.9
	224.3	1.0	5.7

TABLE V: Comparison of experimental results for CaTiO₃ phonon parameters at 6 K with first-principles (FP) results. Frequencies are in cm⁻¹.

Expt.	Expt.	FP	FP	FP
ν	$\Delta\epsilon$	symmetry	ν	$\Delta\epsilon$
67.7	295.05	$1B_{3u}; 1B_{1u}$	85.3; 86.8	177.0
124.3	42.20	$1B_{2u}; 2B_{1u}$	103.6; 111.8	75.66
159.8	0.40	$2B_{3u}$	159.8	2.52
172.9	7.83	$2B_{2u}$	161.0	4.64
180.8	4.55	$3B_{1u}$	171.0	3.48
		$3B_{3u}$	199.2	0.46
224.3	1.86	$3B_{2u}$	216.9	0.23
259.9	0.94	$4B_{2u}; 4B_{1u}$	250.3; 250.7	0.53
		$4B_{3u}$	271.1	0.00003
304.9	0.25	$5B_{2u}$	294.3	0.47
321.7	0.55	$5B_{3u}$	310.8	0.31
		$6B_{2u}$	332.1	0.02
376.1	0.09	$6B_{3u}$	361.6	0.05
435.5	0.48	$5B_{1u}; 7B_{3u}$	422.7; 423.8	0.48
		$6B_{1u}$	468.1	0.0007
494.9	0.11	$7B_{2u}$	479.6	0.07
		$8B_{3u}$	482.7	0.0005
548.6	1.24	$8B_{2u}; 7B_{1u}; 9B_{3u}$	504.5; 507.7; 525.2	1.34
		$9B_{2u}$	546.0	0.004
642.1	0.01			